RSC Advances

ROYAL SOCIETY OF CHEMISTRY

www.rsc.org/advances

Photoluminescence Profile Mapping of Eu(III) and Tb(III → IV)-Embedded in Quantum Size SnO_2 Nanoparticles

Young In Choi and Youngku Sohn*

Department of Chemistry, Yeungnam University, Gyeongsan, Gyeongbuk 712-749, South Korea

Abstract

Eu(III) and Tb(IV) activators were embedded in quantum size SnO_2 nanoparticles by a hydrothermal method and their morphologies, crystal structures and spectroscopic properties were examined by transmission electron microscopy, X-ray diffraction crystallography, UV-visible absorption, and 2D/3D-photoluminescence mapping. Eu(III) embedment showed strong red emissions between 570 and 720 nm, which were attributed to the $^5D_0 \rightarrow {}^7F_J$ (J=0,1,2,3,4) transitions. The magnetic dipole $^5D_0 \rightarrow {}^7F_1$ transition was dominated by an indirect charge transfer excitation, which was attributed to Eu(III) doped at centrosymmetric sites. Conversely, the electric dipole $^5D_0 \rightarrow {}^7F_2$ transition was dominated by direct excitation of Eu(III), which was attributed to Eu(III) at low symmetry sites. Tb(III) was oxidized to Tb(IV) in SnO_2 and showed no characteristic green emissions. A full understanding of the photoluminescence mechanism of Eu(III) and Tb(IV) in SnO_2 will provide new insights into the development of SnO_2-based phosphor materials.

* Corresponding author e-mail: youngkusohn@ynu.ac.kr
Tel: +82-53-810-2354; Fax: +82-53-810-4613

Key words: SnO_2; Eu(III); Tb(III,IV); quantum size; photoluminescence map

Introduction

Tin oxide (SnO_2) with a wide bad gap of around 3.6 eV has attracted a great deal of attention owing to its unique properties and potential for use in sensors, solar cells, electronics and catalysts.[1-10] The fundamental properties of SnO_2 are highly dependent on many factors, including size and morphology. Accordingly, various synthetic methods have been employed to synthesize SnO_2 with diverse morphologies, including quantum dots, triangles, nanosheets, cubes, nanobelts and nanowires/needles.[11-20] The synthetic methods include hydrothermal, sol-gel/spin-coating, sol-gel, microemulsion, microwave-assisted solvothermal methods, and chemical vapor deposition. Luwang et al. synthesized triangular Eu(III)-doped SnO_2 nanoparticles using a microemulsion route.[12] Zeferino et al. synthesized Eu-doped (0.5, 1.0 and 2.0%) SnO_2 nanoparticles (4–11 nm in size) by a hydrothermal method (NaOH base, 190°C and 24 h).[21] Bhaktha et al. prepared Eu(III)-doped $(100-x)SiO_{2-x}SnO_2$ nanomaterials by a sol-gel dip-coating method as low-loss optical waveguides.[22] The hydrothermal method has been widely employed for synthesis of SnO_2 with various morphologies by varying surfactants, pHs, temperatures and reaction solvents.[13,15,16,19,20] SnO_2-based materials have been extensively used as supports for improving luminescence efficiency.[22,23] Eu(III) ions are the materials that have been most extensively used for development of red phosphor materials due to their unique $^5D_0 \rightarrow {}^7F_J$ (J=0,1,2,3,4) transition emission. Luminescence of Eu(III) has been used as a probe for material characterization (e.g., size estimation) and biomedical application (e.g., cell imaging and drug location).[24-26] Strauss et al. demonstrated that SnO_2 particle size could be probed by Eu^{3+} luminescence. Specifically, they found that electric dipole transition was decreased relative to the magnetic dipole transition as the particle size increased.[24] These characteristics were attributed to the relative decrease of Eu^{3+} in surface sites. Huang et al. synthesized SnO_2:Eu^{3+} phosphor and demonstrated that it was useful in a field emission display exhibiting orange-red color.[27]

Studies conducted to date have primarily focused on doping-concentration and annealing temperature dependent photoluminescence profiles, and used one (or two) excitation wavelengths to take emission spectra.[14,21,22,28,24,29] As a result, there is no detailed excitation-wavelength dependent information currently available. The present study further demonstrates excitation-wavelength dependent photoluminescence profiles

of Eu(III)-doped quantum size SnO_2 nanoparticles with annealing temperature. Photoluminescence (PL) profile mapping of the Eu(III) and Tb(IV)-doped SnO_2 nanoparticles was then performed to clarify the fundamental photoluminescence characteristics.

Materials and methods

Eu(III) and Tb(IV)-doped SnO_2 nanoparticles were synthesized by a hydrothermal method. Briefly, we added 10.0 mL of 0.1 M $SnCl_4 \cdot 5H_2O$ (98%, Sigma-Aldrich Co.) and an appropriate amount (0.1 and 1.0 mL for 1 and 10.0 mol% doping, respectively) of 0.1 M Eu(III)$NO_3 \cdot 6H_2O$ (or 0.1 M Tb(III)$NO_3 \cdot 6H_2O$) solution into 20.0 mL of Millipore water and stirred the samples for 10 min. We next added 4.0 mL of 0.1 M NaOH solution to obtain precipitates. The solution with precipitates was placed in a Teflon bottle, tightly sealed and placed in an oven at 120°C for 12 hours. The final white products were washed with ethanol and deionized water, then fully dried at 80°C. We heat-treated the powder samples in air at 700°C for 4 hours and naturally cooled to room temperature. The surface morphology was examined by transmission electron microscopy (TEM, Hitachi H-7600) operated at 100 kV for the samples placed on a carbon-coated Cu grid. X-ray diffraction (XRD) patterns of the powder samples were taken using a PANalytical X'Pert Pro MPD diffractometer with Cu Kα radiation (40 kV and 30 mA). For the as-prepared and annealed powder samples, UV-Vis absorption spectra were obtained using a SCINCO NeoSys-2000 double beam UV–Vis spectrophotometer. A Thermo Scientific Nicolet iS10 spectrometer was used to record the Fourier transform infrared (FT-IR) spectra. Photoluminescence (PL) profiles of the power samples were obtained using a SCINCO FluoroMate FS-2 at room temperature (20 ~ 25°C). To minimize the effects of powder distribution/amount on PL intensity, we used the same amount (30 mg) of power sample and mounted on a specially-designed sample holder (Supporting Information, Fig. S1). The holder was designed to allow accurate PL measurement for powder sample. To obtain 2D/3D-PL profile map, we collected photoemission (540 – 720 nm) spectra for a broad range of excitation wavelengths of 250 – 420 nm. Since we used excitation wavelengths with 5 nm intervals, the number of .collected photoemission spectra was 171. The PL profile map was then automatically generated by a FluoroMater Plus software.

Results and Discussion

Figure 1 shows typical TEM images of as-prepared and 700°C-annealed Eu(III)/SnO_2 and Tb(IV)/SnO_2 nanoparticles. The as-prepared nanoparticles were found to be extremely small, with diameters of 2–3nm. Upon annealing at 700°C, the quantum size[11] nanoparticles became aggregated to form a larger island, with estimated particle diameters of ~10nm. The Eu(III) and Tb(IV)-doped samples showed very similar morphologies.

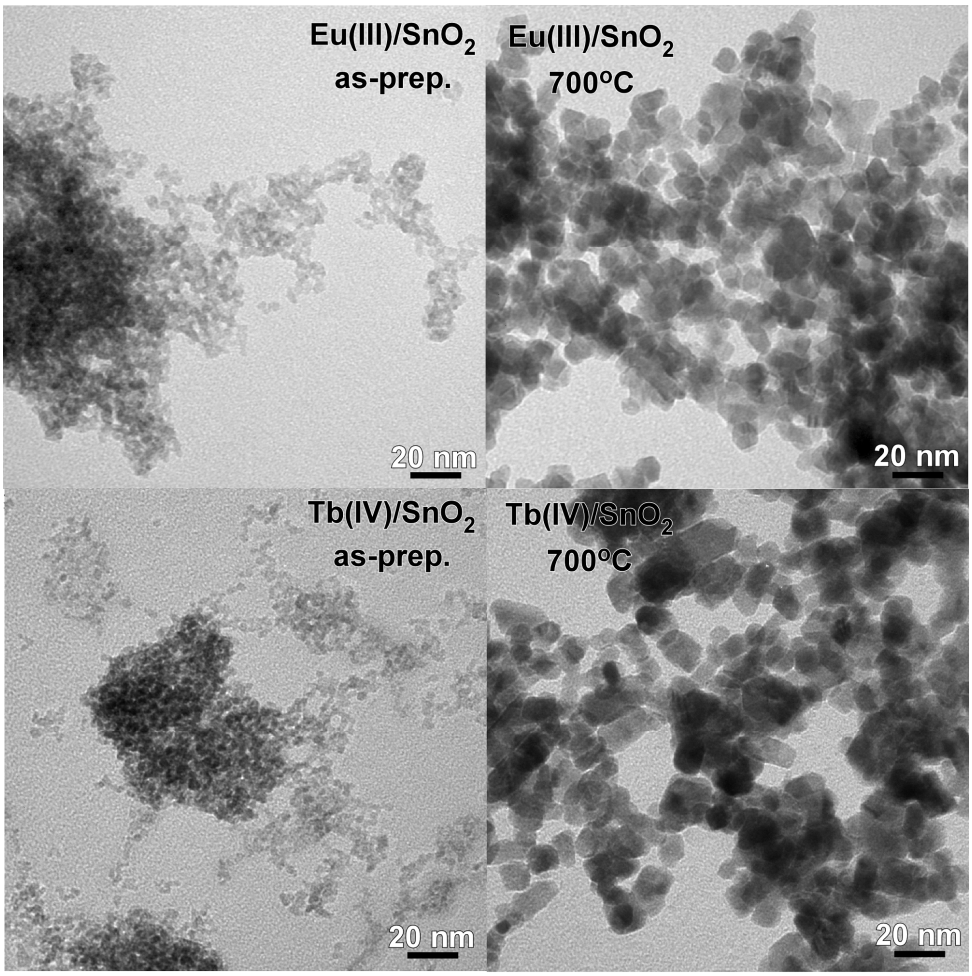

Figure 1. Typical TEM images of as-prepared and 700°C-annealed Eu(III)/SnO_2 and Tb(IV)/SnO_2 nanoparticles.

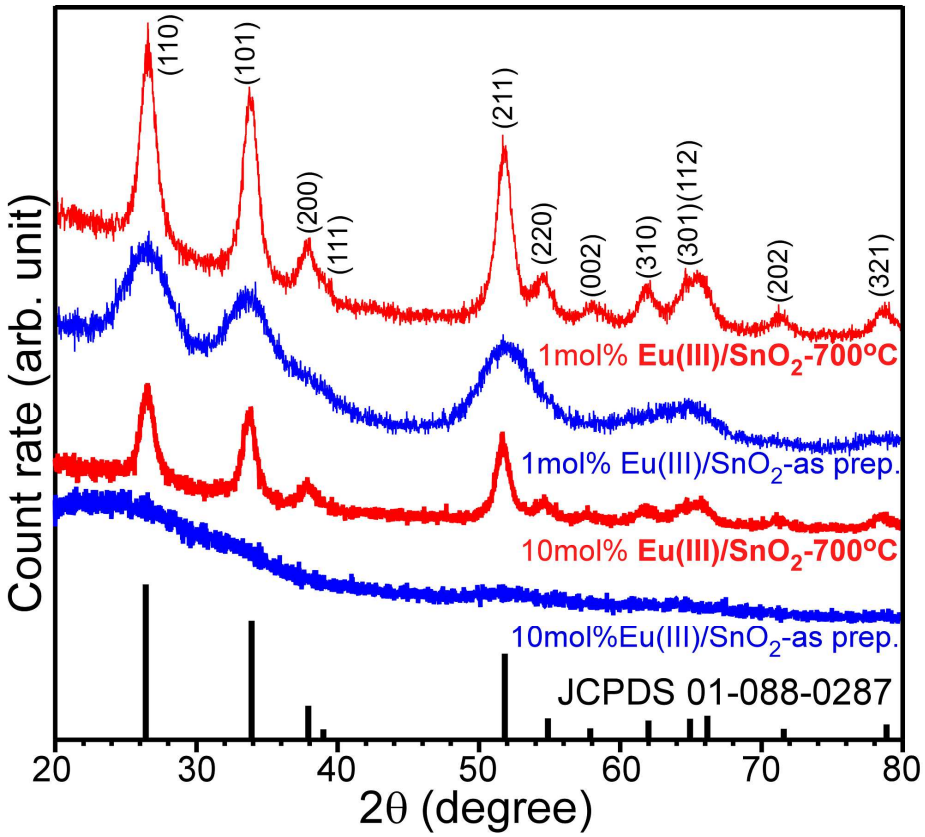

Figure 2. Power X-ray diffraction patterns of as-prepared and 700°C-annealed 1 and 10mol% Eu(III)/SnO_2 nanoparticles, and a reference XRD pattern.

Figure 2 displays power X-ray diffraction patterns of as-prepared and 700°C-annealed 1 and 10mol% Eu(III)/SnO_2 nanoparticles. The XRD peaks of the as-prepared 1mol% Eu(III)-doped samples were broad, reflecting extremely small sizes of the sample. However, the XRD peaks became sharper upon annealing at 700°C, indicating that the particle size and crystallinity increased. The XRD peak patterns were in good agreement with those of tetragonal (P42/mnm) SnO_2 (JCPDS 01-088-0287). The three most dominant peaks at 2θ=26.6º, 33.9º and 51.8º were assigned to the (110), (101), and (211) planes, respectively. Other peaks were assigned as shown in Figure 2. During the hydrothermal reaction, it was expected that Sn^{4+} would react with OH^- to form Sn hydroxides,[13] which are then dehydrated to produce quantum size SnO_2 nanoparticles. However, we found no XRD patterns of $Eu_2Sn_2O_7$ after thermal annealing.[28] For the as-prepared 10mol% Eu(III)-doped sample, no significant XRD peaks were observed due to an amorphous state. However, the crystallinity was recovered after thermal annealing.

For the 1mol% Eu(III)-doped sample, we estimated the particle sizes before and after thermal annealing using the Debye–Scherrer equation ($D = 0.9\lambda/\beta\cos\theta$, where λ is the X-ray wavelength, β is the half-width of the XRD peak, and θ is the angle).[11,12,18] We selected the strongest peak at $2\theta=26.6^{o}$ corresponding to the (110) plane and measured the full-width at half maximum. The sizes were calculated to be 2.4 nm and 7.5 nm before and after thermal annealing, which is in good agreement with the sizes estimated from the TEM images.

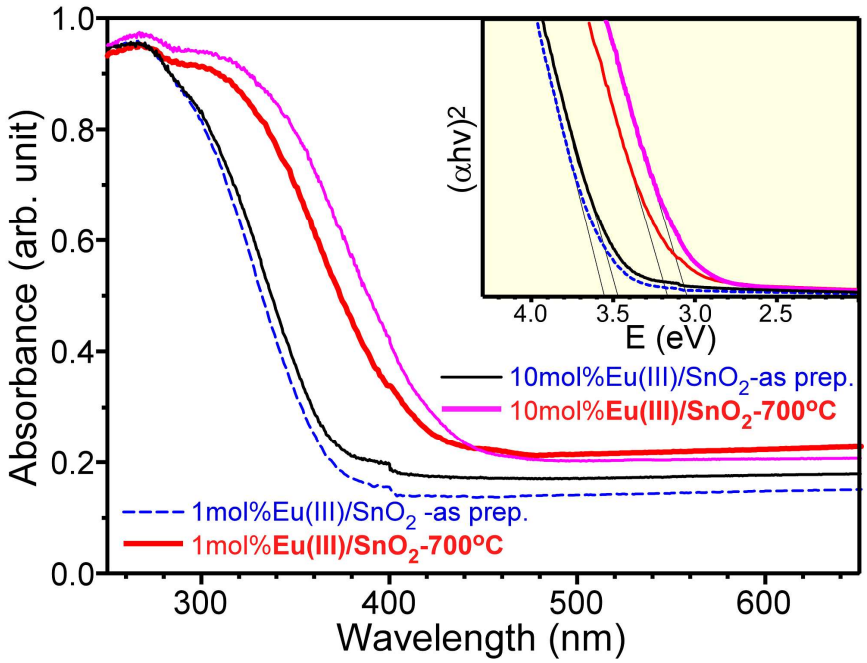

Figure 3. UV-Vis absorption spectra of as-prepared and 700°C-annealed 1 and 10 mol% Eu(III)/SnO_2 nanoparticles.

Figure 3 displays UV-visible absorption spectra of as-prepared and 700°C-annealed Eu(III)/SnO_2 nanoparticles. The absorption edge was clearly shifted to a longer wavelength upon thermal annealing, which is consistent with previously published results.[29] Kar and Patra prepared Eu(III)-doped SnO_2 nanocrystals by a microwave technique and found that the absorption edge was deceased with increasing annealing temperature.[29] The band gaps (E_g) were estimated using the Tauc equation, $\alpha h\nu = k(h\nu - E_g)^{n/2}$, where α is the optical absorption coefficient, k is an empirical constant, and n = 4 and 1 for indirect and direct band gaps, respectively.[11,12] The direct absorption band gaps for the 1mol% Eu(III)-doped SnO_2 were measured to be 3.56 and 3.18 eV before and after

annealing. For the as-prepared 10 mol% Eu(III)-doped sample, the band gap was measured to be 3.48 eV, which was ~0.1 eV smaller than that of the as-prepared 1mol% Eu(III)-doped SnO_2. It has generally been observed that band gap decreases with increasing doping concentration. This could be explained that guest ions create energy levels near the band edges, and as a consequence the band gap is decreased. After thermal annealing, the band gap was measured to be 3.06 eV, which was 0.42 eV smaller than that of the as-prepared sample. The decrease in band gap is plausibly due to increase in particle size after thermal annealing (Figure 1). Band gaps are commonly found to increase with decreasing particle sizes due to a quantum confinement effect.[24] Bazargan and Leung reported band gaps of 4.7 and 4.22 eV for pure and 10% Eu(III)-doped (500°C-annealed) SnO_2 films, respectively,[28] while Sanchez Zeferino et al. reported band gaps between 3.80 and 3.90 eV for Eu-doped (0.5, 1.0 and 2.0%) SnO_2 nanoparticles[21] and Wang et al. reported band gaps of 3.72 -3.80 eV for Eu(III)-doped SnO_2 nanoparticles with a diameter of 3-7 nm.[30]

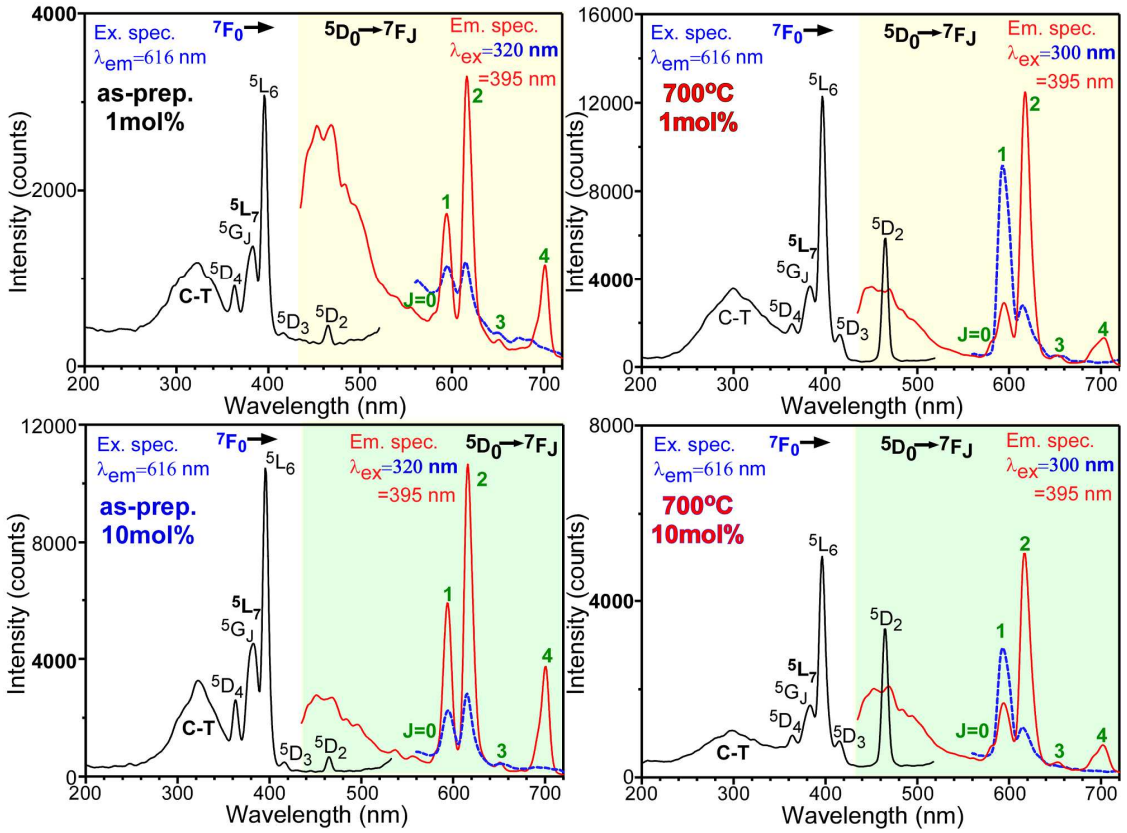

Figure 4. Excitation and emission spectra of as-prepared (left) and 700°C-annealed (right) 1 (top) and 10 mol% (bottom) Eu(III)/SnO_2 nanoparticles.

FT-IR spectra (Supporting Info. Fig. S2) were examined for the as-prepared and annealed samples. A strong and broad peak was commonly found at 3300 cm^{-1}, which was ascribed to OH stretching due to adsorbed water.[18,12,31] Upon annealing at 700°C, the broad peak was significantly suppressed due to removal of adsorbed OH species after thermal annealing.

Figure 4 displays the excitation and emission spectra of the as-prepared and 700°C-annealed 1 and 10mol% Eu(III)-doped SnO_2 nanoparticles. We recorded the excitation spectra at an emission wavelength of 616 nm, which was attributed to the $^5D_0 \rightarrow {}^7F_2$ transition. For the as-prepared 1 mol% Eu(III)/SnO_2 samples, the sharp peaks were attributed to f-f transitions as summarized in Table 1. The broad band at 320 nm was attributed to the O^{2-}– Eu^{3+} charge transfer[12] related to the interband electronic transition of SnO_2.[22] For the 1 mol% Eu(III)/SnO_2 sample, the intensities were dramatically enhanced upon annealing at 700°C, while the excitation spectral profile was somewhat changed. The major sharp peaks showed no change in peak position, while the charge transfer band was shifted to a shorter wavelength of 300 nm, which was accompanied by an increase (3.5×) in intensity. The $^5L_6 \leftarrow {}^7F_0$ excitation transition peak at 395 nm was increased by 4.3× after thermal annealing, while the $^5D_2 \leftarrow {}^7F_0$ excitation transition peak at 465 nm was more dramatically enhanced by >18.8×.

Table 1. Upper energy levels $\leftarrow {}^7F_0$ excitation transitions for as-prepared 1mol% Eu(III)-doped sample.

Upper energy levels	$^5D_4$	$^5G_J/{}^5L_7$	$^5L_6$	$^5D_3$	$^5D_2$
as-prep. (1mol%)	363 nm	382 nm	396 nm	416 nm	465 nm

Table 2. $^5D_0 \rightarrow {}^7F_J$ emission transitions for as-prepared 1mol% Eu(III)-doped sample.

J	0	1	2	3	4
as-prep. (1mol%)	579.7 nm	594.0 nm	616.6 nm	650.9 nm	701.0 nm

We selected two different wavelengths to generate emission spectra for the as-prepared samples (320 and 395 nm), and for the annealed samples (300 and 395).

Wavelengths 320 and 300 nm correspond to the those centered at the charge transfer bands for the as-prepared and annealed samples, respectively. This excitation wavelength is referred to as indirect excitation. The 395 nm wavelength corresponds to the $^5L_6 \leftarrow {}^7F_0$ excitation transition of Eu(III), and is referred to as a direct transition wavelength. Sharp emission peaks were commonly found between 560 and 720 nm and associated with the following transitions of the Eu(III) ion: $^5D_0 \rightarrow {}^7F_J$ (J = 0,1,2,3,4) summarized in Table 2. A broad emission peak was observed at 460 nm, which was attributed to oxygen defects present in the SnO_2 support.[21] Interestingly, the emission profile taken at λ_{ex} = 395 nm differed significantly from that taken at the indirect excitation wavelength (λ_{ex} = 300 or 320 nm). For the emission spectrum at λ_{ex} = 300 nm of the as-prepared sample, the emission peak at 616 m was much stronger than that at 594 nm. However, for the spectrum at λ_{ex} = 320 nm, the emission peak at 594 nm was comparable to that at 616 nm. The $I(^5D_0 \rightarrow {}^7F_2)/I(^5D_0 \rightarrow {}^7F_1)$ asymmetric ratios were observed to be 1.45 and 2.15 at excitation wavelengths of 300 and 395 nm, respectively (Table 3). Upon annealing at 700°C, the emission peaks were much more enhanced than those of as-prepared samples. The broad emission at 470 nm was increased by 1.36×, while the sharp emission peak at 616 nm obtained at λ_{ex} = 395 nm was increased by 4.2× and the emission peak at 594 nm obtained at an indirect excitation wavelength was increased by 21.2×. For the annealed samples, the asymmetric ratios were measured to be 0.27 and 4.78 at λ_{ex} = 300 nm (indirect excitation) and 395 nm (direct excitation), respectively (Table 3). Since high symmetric Eu(III) is mainly sensitized by the indirect excitation the $^5D_0 \rightarrow {}^7F_1$ transition emission will be observed to be stronger than the $^5D_0 \rightarrow {}^7F_2$ emission to give a lower asymmetric ratio (Supporting Info. Fig. S3). On the other hand, since low symmetric Eu(III) is efficiently sensitized by the direct excitation the $^5D_0 \rightarrow {}^7F_2$ transition emission will be observed to be stronger than the $^5D_0 \rightarrow {}^7F_1$ emission to give a higher asymmetric ratio.

Table 3. Summarized asymmetric ratios.

Asymmetric ratio	As-prepared (1 mol / **10 mol%)**	700°C-annealed (1mol / **10 mol%**)

λ_{ex} = 320/**300 nm**	1.45/**1.50**	0.27/**0.30**
λ_{ex} = 395 nm	2.15/**1.87**	4.78/**3.43**

The excitation and emission profiles of the as-prepared and annealed 10 mol% Eu(III)/SnO_2 samples were very similar to those of the 1 mol% Eu(III)/SnO_2 samples, except for the peak intensities and relative intensities. The excitation and emission peaks were already assigned as discussed above. For the excitation spectrum of the as-prepared 10 mol% Eu(III)/SnO_2 sample, the $^5L_6 \leftarrow {}^7F_0$ excitation transition peak at 395 nm was increased by 3.5× relative to that of the 1 mol% Eu(III)/SnO_2 sample. Lee et al. prepared SnO_2:Eu^{3+} phosphors with different doping concentrations and commonly observed a stronger $^5D_0 \rightarrow {}^7F_1$ transition peak relative to the $^5D_0 \rightarrow {}^7F_2$ transition at a fixed excitation wavelength of 314 nm, as well as an enhancement of luminescent intensity with doping concentration.[14] However, upon annealing at 700°C, the peak intensity at 395 nm was decreased by 0.48×. The decrease in intensity may have been due to a quantum size effect, or to the formation of $Eu_2Sn_2O_7$ after thermal annealing.[32,29,28] Psuja et al. observed a decrease in PL intensity after annealing at above 1300°C, which was attributed to phase separation.[32] Bazargan and Leung also reported that Eu and SnO_2 formed $Eu_2Sn_2O_7$ after annealing at above 700°C, which suppresses Eu(III) emission.[28]

For the as-prepared 10 mol% Eu(III)-doped SnO_2 sample, the asymmetric ratios were measured to be 1.50 and 1.87 at λ_{ex} = 300 and 395 nm, respectively (Table 3). Upon annealing at 700°C, the ratio was found to be 0.30 and 3.43, respectively. For 1 and 10 mol% Eu(III)/SnO_2 samples, the asymmetric ratio measured at the indirect excitation wavelength was significantly lower (~0.2×) after thermal annealing, indicating that the charge transfer efficiency from SnO_2 to Eu(III) with high symmetry increased, or more Eu(III) ions are likely doped at high symmetry sites after thermal annealing.[33] However, the ratios at the direct excitation wavelength were increased by ~2×. As the doping concentration increased from 1 to 10 mol%, the asymmetric ratio increased slightly by 1.05× at the indirect excitation wavelength. Conversely, the ratio was decreased by 0.8× at the direct excitation wavelength of 395 nm. Literature reports on asymmetric ratios for Eu(III)-doped SnO_2 were summarized in Table 4.

Table 4. Summary of literature reports on asymmetric ratios.

Wang et al.[30]	asymmetric ratios of 1.44 and 0.95 for 10.0 and 2.5 mol% Eu(III)-doped SnO_2 nanoparticles
Sanchez Zeferino et al.[21]	$^5D_0 \rightarrow {}^7F_1$ transition was predominant relative to $^5D_0 \rightarrow {}^7F_2$ transition at a fixed λ_{ex} = 325 nm for Eu-doped (0.5, 1.0 and 2.0%) SnO_2 nanoparticles (4–11 nm in size)
Nogami et al.[17]	$^5D_0 \rightarrow {}^7F_2$ transition emission peak was stronger than $^5D_0 \rightarrow {}^7F_1$ transition at λ_{ex} = 337 nm for 1wt% Eu(III)-doped SnO_2-SiO_2 glasses prepared by a sol-gel method.
Bajpai et al.[18]	$^5D_0 \rightarrow {}^7F_1$ transition was stronger than the $^5D_0 \rightarrow {}^7F_2$ transition at λ_{ex} = 395 nm for 0.5 mol% Eu(III)-doped SnO_2 nanoparticles (~15.6 nm) prepared by a sol-gel method.
Yu et al.[34]	asymmetric ratio was much smaller for 0.5 mol% Eu(III)-doped SnO_2 nanocrystals at an indirect λ_{ex} = 335 nm than that obtained at a indirect λ_{ex} = 465 nm.
Zhang et al.[31]	for 400 and 1000°C-annealed SnO_2:Eu samples, emission spectra at λ_{ex} = 300 nm, the $^5D_0 \rightarrow {}^7F_1$ transition became dominant after annealing at 1000°C, with an asymmetric ratio of ~0.25. Emission spectra at λ_{ex} = 395 nm, the $^5D_0 \rightarrow {}^7F_2$ transition became comparable to the $^5D_0 \rightarrow {}^7F_1$ transition, and the asymmetric ratio was decreased after annealing to 1000°C.
Wei et al.[33]	$^5D_0 \rightarrow {}^7F_1$ and $^5D_0 \rightarrow {}^7F_2$ transitions and the asymmetric ratio all decreased with increasing sample temperature, attributed to an increase in phonon-assisted non-radiative recombination. $^5D_0 \rightarrow {}^7F_2$ transition more sensitively influenced by the sample temperature.

It is well known that the $^5D_0 \rightarrow {}^7F_1$ transition is magnetic dipole allowed and insensitive to local site symmetry, while the $^5D_0 \rightarrow {}^7F_2$ transition is electric dipole allowed and very sensitive to the local symmetry. The electric dipole transition is forbidden when Eu(III) is doped at a centrosymmetric site.[22] Based on our observations, charge transfer excitation only efficiently sensitizes the Eu^{3+} doped at centrosymmetric

sites.[33-35] In the SnO_2 support, Eu^{3+} is replaced with Sn^{4+} to have local C_{2h} or D_{2h} symmetry sites.[14,33] In other words, the Eu^{3+} doped at Sn^{4+} can be efficiently sensitized by the indirect excitation.[34] The other Eu^{3+} ions may be doped at low symmetry sites and sensitized by direct excitation at 395 nm. Zeferino et al. reported that, since the size of Eu^{3+} ions is bigger than that of Sn^{4+} ions, the Eu^{3+} was more likely embedded at the interstitial sites of SnO_2 support.[21] However, Yu et al. concluded that, although the radius (0.095 nm) of Eu^{3+} is bigger than that (0.076 nm) of Sn^{4+}, some Eu^{3+} ions could be embedded into the SnO_2 matrix at the C_{2h} or D_{2h} symmetry site.[34] Yu et al. measured a longer lifetime of 8.4 ms for the ($^5D_0 \rightarrow {}^7F_1$) transition emission than 1.9 ms for the $^5D_0 \rightarrow {}^7F_2$ transition emission.[34] In other words, the Eu^{3+} ions with high symmetry sites exhibited a longer lifetime than those with low symmetry. Bazargan and Leung prepared Eu(III)-doped SnO_2 films with doping concentrations up to 20%[28] and examined photoluminescence at a fixed excitation wavelength of 300 nm. They found that, as the doping concentration increased, the emission at 614 nm became more pronounced than the emission at 593 nm. This was explained by Eu(III) occupying centrosymmetric sites (e.g., C_{2h} symmetry) at low doping concentrations, while it became positioned at non-centrosymmetric sites at high doping concentrations.

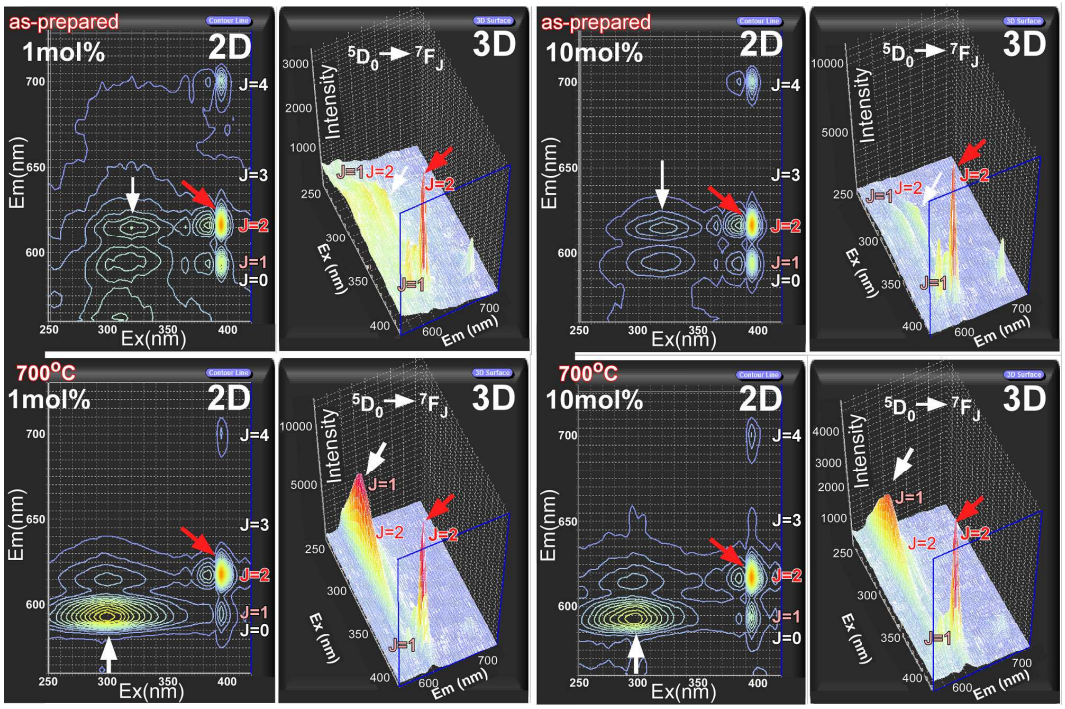

Figure 5. 2D and 3D photoluminescence profile map of as-prepared and 700°C-annealed 1 (left two columns) and 10 mol% (right two columns) Eu(III)/SnO_2 nanoparticles. Ex and Em indicate excitation and emission wavelengths, respectively. Z-axis in the 3D map is emission intensity.

Figure 5 shows the corresponding 2D and 3D photoluminescence profile map[36-39] of as-prepared and 700°C-annealed 1 and 10 mol% Eu(III)/SnO_2 nanoparticles. As shown in the profile map, the more densely spaced contour region indicates a stronger signal. The PL map became clearly different before and after thermal annealing. For the as-prepared samples, the densely spaced region was localized at the $^5D_0 \rightarrow {}^7F_2$ transition emission (marked by red arrows) by a direct excitation of 395 nm. For the annealed samples, the contour lines were localized at the $^5D_0 \rightarrow {}^7F_1$ transition emission (marked by white arrows) by an indirect excitation of 300 nm, and at the $^5D_0 \rightarrow {}^7F_2$ transition emission (marked by red arrows) by a direct excitation of 395 nm. Additionally, the emission profiles were highly excitation wavelength dependent. Taken together, these findings confirm that Eu(III) are doped at both centrosymmetric and non-centrosymmetric sites.

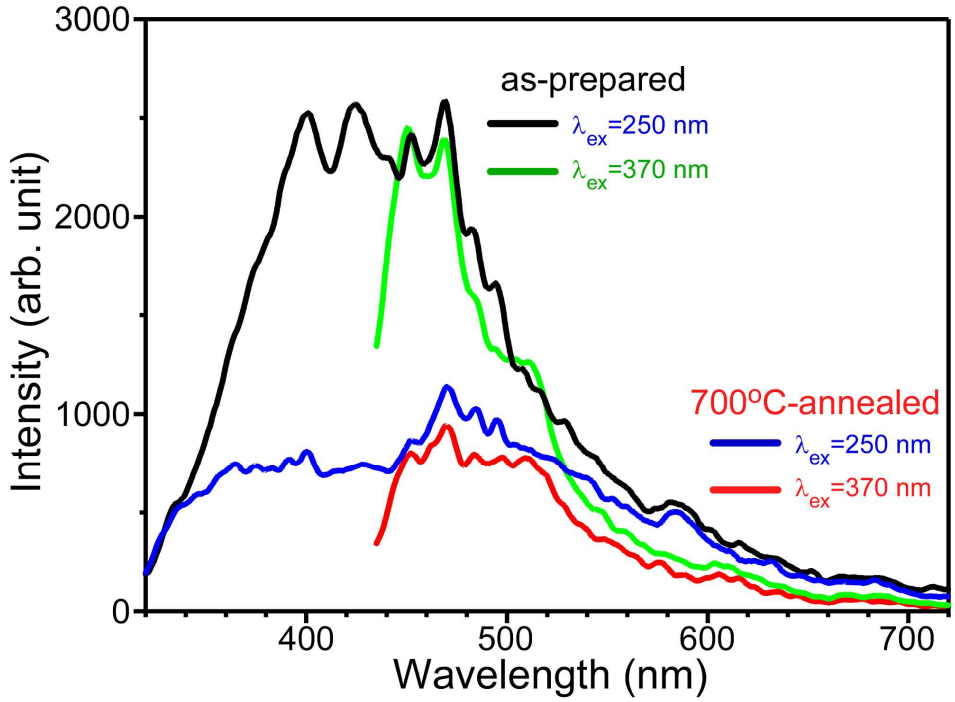

Figure 6. Emission spectra of as-prepared and 700°C-annealed 10mol% Tb(IV)/SnO_2 nanoparticles.

Figure 6 shows the emission spectra of as-prepared and 700°C-annealed Tb(IV)/SnO_2 nanoparticles taken at excitation wavelengths of 250 (indirect excitation) and 370 nm (direct excitation). Interestingly, we commonly observed broad emission peaks with no characteristic sharp $^5D_4 \rightarrow {}^7F_J$ (J = 6, 5, 4, 3) transition emissions of Tb(III) although we used Tb(III) ions for doping. These findings indicate that Tb(III) is oxidized to non-luminescent Tb(IV), or not efficiently sensitized in the SnO_2 matrix. A similar observation was also found for Tb(III) in CeO_2, and Y_2O_3 matrices.[38,39] To confirm this, we measured UV-Vis absorption spectra (Supporting Info. Fig. S4) for the Tb-doped samples. We observed an enhanced UV-Vis absorption at 440 nm, attributed to $O^{2-} \rightarrow Tb^{4+}$ charge transfer absorption.[38-42] This clearly indicates that the oxidation state of Tb(III) was changed to non-luminescent Tb(IV) in SnO_2 matrix. It was also found that Tb(III) was oxidized to Tb(IV) in MO-Al_2O_3 (M=Mg, Ca, Sr, Ba) and La_2O_3 matrices.[40-42] The broad emission peak consists of several peaks, attributed to various defects (e.g., surface/bulk, F^0, F^+ and F^{++} centers).[43-45] The broad emission peak was decreased after thermal annealing due to a decrease in defect sites.

Conclusions

A hydrothermal synthetic method was successfully employed to embed Eu(III) into quantum size SnO_2 nanoparticles. Photoluminescence profile mapping was used to fully understand photoluminescence profiles dependent on excitation wavelengths. For the Eu(III)/SnO_2 sample, various emission peaks were found between 570 and 720 nm and attributed to the $^5D_0 \rightarrow {}^7F_J$ (J=0,1,2,3,4) transition. However, Tb(III) in SnO_2 showed no $^5D_4 \rightarrow {}^7F_J$ (J = 6, 5, 4, 3) transition emission. This indicates that Tb(III) was oxidized to Tb(IV) in the oxide matrix. The $I(^5D_0 \rightarrow {}^7F_2)/I(^5D_0 \rightarrow {}^7F_1)$ asymmetric ratios were slightly dependent on doping concentrations, but were found to be highly dependent on excitation wavelength and annealing temperature. The magnetic dipole $^5D_0 \rightarrow {}^7F_1$ and the electric dipole $^5D_0 \rightarrow {}^7F_2$ transitions were dominated by an indirect charge transfer and direct Eu(III) excitations, respectively. These results indicated that Eu(III) was doped at centrosymmetric and non-centrosymmetric sites. For the as-prepared sample, the $^5D_0 \rightarrow {}^7F_2$ transition was more dominant than the $^5D_0 \rightarrow {}^7F_1$ transition. Upon annealing at 700°C, the $^5D_0 \rightarrow {}^7F_1$ transition became comparable to the $^5D_0 \rightarrow {}^7F_2$ transition. Although there

is a charge unbalance and a size difference between Eu^{3+} and Sn^{4+}, some Eu(III) activators appeared to be doped at high symmetry sites. As a result, good charge transfer occurred from SnO_2 to Eu^{3+} to emit the $^5D_0 \rightarrow {}^7F_1$ transition emission. This charge transfer was enhanced by thermal annealing. Overall, photoluminescence profile map provides deeper insights enabling a better understanding of photoluminescence mechanisms that can facilitate development of SnO_2-based phosphor materials.

Acknowledgement. This work was supported by a National Research Foundation of Korea (NRF) grant funded by the Korean government (MEST) (2012R1A1A4A01005645).

References

1. J. S. Chen and X. W. Lou, *Small*, 2013, **9**, 1877-1893.

2. C. Wang, G. Du, K. Stahl, H. Huang, Y. Zhong and J. Z. Jiang, *J. Phys. Chem. C.*, 2012, **116**, 4000-4011.

3. S. Gubbala, H. B. Russell, H. Shah, B. Deb, J. Jasinski, H. Rypkema and M. K. Sunkara, *Energy Environ. Sci.,* 2009, **2**, 1302–1309.

4. H. You, Rui Liu, C. Liang, S. Yang, F. Wang, X. Lu and B. Ding, *J. Mater. Chem. A*, 2013, **1**, 4097–4104.

5. G. Xi and J. Ye, *Inorg. Chem*., 2010, **49**, 2302–2309.

6. P. Sun, W. Zhao, Y. Cao, Y. Guan, Y. Sun and G. Lu, *CrystEngComm*, 2011, **13**, 3718–3724.

7. C. Jiang, G. Zhang, Y.Wu, L. Li and K. Shi, *CrystEngComm*, 2012, **14**, 2739-2747.

8. A. Kar, S. Kundu and A. Patra, *J. Phys. Chem. C.*, 2011, **115**, 118-124.

9. S. Liu, G. Huang, J. Yu, T. W. Ng, H. Y. Yip and P. K. Wong, *ACS Appl. Mater. Interfaces*, 014, **6**, 2407–2414.

10. X. Wang, L. Xiao,H. Peng, W. Liu and X. Xu, *J. Mater. Chem. A*, 2014, **2**, 5616-5619.

11. S. Sharma, A. K. Srivastava and S. Chawla, *Appl. Surf. Sci*., 2012, **258,** 8662– 8666.

12. M. N. Luwang, *Appl. Surf. Sci.,* 2014, **290**, 332– 339.

13. O. Lupan, L. Chow, G. Chai, A. Schulte, S. Park and H. Heinrich, *Mater. Sci. Eng. B*, 2009, **157**, 101-104.

14. C. -T. Lee, F. -S. Chen and C. -H. Lu, *J. Alloys Compd.*, 2010, **490**, 407–411.

15. H. Zhu, D. Yang, G. Yu, H. Zhang and K.Yao, *Nanotechnol*., 2006, **17**, 2386–2389.

16. H. Uchiyama, Y. Shirai and H. Kozuka, *RSC Advances*, 2012, **2**, 4839–4843.

17. M. Nogami, T. Enomoto and T. Hayakawa, *J. Lumin.*, 2002, **97**, 147–152.

18. N. Bajpai, S. A. Khan, R. S. Kher, N. Bramhe, S. J. Dhoble and A. Tiwari, *J. Lumin.*, 2014, **145**, 940–943.

19. L. Yu, L.Zhang, H. Song, X. Jiang and Y. Lv, *CrystEngComm*, 2014,**16**, 3331-3340.

20. O. Acarbas, E. Suvaci and A. Dogan, *Ceram. Inter*., 2007, **33**, 537-542.

21. R. Sanchez Zeferino, U. Pal, R. Melendrez, H. A. Duran-Munoz and M. Barboza Flores, *J. Appl. Phys.*, 2013, **113**, 064306/1-6.

22. S. N. B. Bhaktha, F. Beclin, M. Bouazaoui, B. Capoen, A. Chiasera, M. Ferrari, C. Kinowski, G. C. Righini, O. Robbe and S. Turrell*, Appl. Phys. Lett.*, 2008, **93**, 211904/1-3.

23. H. Wang, Y. Wang, S. V. Kershaw, T. F. Hung, J. Xu and A. L. Rogach, *Part. Part. Syst. Charact.*, 2013, **30**, 332–337.

24. M. Strauss, T. A. Destefani, F. A. Sigoli and I.O. Mazali, *Cryst. Growth Des.*, 2011, **11**, 4511–4516.

25. G.Yang, S. Gai, F. Qu and P. Yang, *ACS Appl. Mater. Interfaces*, 2013, **5**, 5788−5796.

26. H. Liu, L. Li, X. -M Tian, W.-Y. Hu, X. -Y. Kuang and Y. –Z. Shao, *Eur. J. Inorg. Chem.,* 2012, **34**, 5677-5684.

27. T. Huang, X. Wang, P. Zhu, H. Li, T. Feng and Z. Sun, *Int. J. Appl. Ceram. Technol.*, 2013, **10**, 625–630.

28. S. Bazargan and K. T. Leung, *J. Chem. Phys.*, 2012, **137**, 184704/1-8.

29. A. Kar and A. Patra, *J. Phys. Chem. C.*, 2009, **113***,* 4375–4380.

30. G. Wang, Y. Yang, Q. Mu and Y. Wang, *J. Alloys Compd.*, 2010, **498**, 81–87.

31. X. Fu, H. Zhang, S. Niu and Q. Xin, *J. Solid State Chem.*, 2005, **178**, 603–607.

32. P. Psuja and W. Strek, *J. Rare Earths*, 2012, **30**, 627–631.

33. Z. Xiao-Wei, L. Tao, X. Jun, X. Ling and C. Kun-Ji, *Chin. Phys. B*, 2012, **21**, 018101/1–7.

34. Y. Yu, D. Chen, P. Huang, H. Lin, A. Yang and Y. Wang, *J. Solid State Chem.*, 2011, **184,** 236–240.

35. M. Nogami and A. Ohno, *J. Non-Cryst. Solids*, 2003, **330**, 264–267.

36. Y. Sohn, *Ceram. Inter.*, 2014, **40**, 2467–2475.

37. Y. Sohn, *Ceram. Inter.*, 2013, **39**, 9157–9161.

38. Y. Sohn, *J. Am. Ceram. Soc.*, 2013, **12,** 3747–3752.

39. I. Cho, J.-G. Kang and Y. Sohn, *Bull. Kor. Chem. Soc.*, 2014, **35**, 575–580.

40. R. K. Verma, K. Kumar and S. B. Rai, Solid State Sci., 2010, **12**, 1146-1151.

41. E. Zych, P. J. Deren, W. Strek, A. Meijerink, W. Mielcarek and K Domangala, J. Alloys Compd., 2001, **323**, 8-12.

42. H. Ebendorff-Heidepriem and D. Ehrt, Opt. Mater., 2000, **15**, 7-25.

43. A. Askrabic, Z. D. Dohcevic-Mitrovic, V. D. Araujo, G. Ionita, M. M. de Lima Jr, A and Cantarero, *J. Phys. D.*, 2013, **46**, 495306/1–9.

44. A. Kar, S. Kundu and A. Patra, *J. Phys. Chem. C.,* 2011, **115**, 118−124.

45. W. Zhou, Y. Liu, Y. Yang and P. Wu, *J. Phys. Chem. C.*, 2014, **118**, 6448−6453.

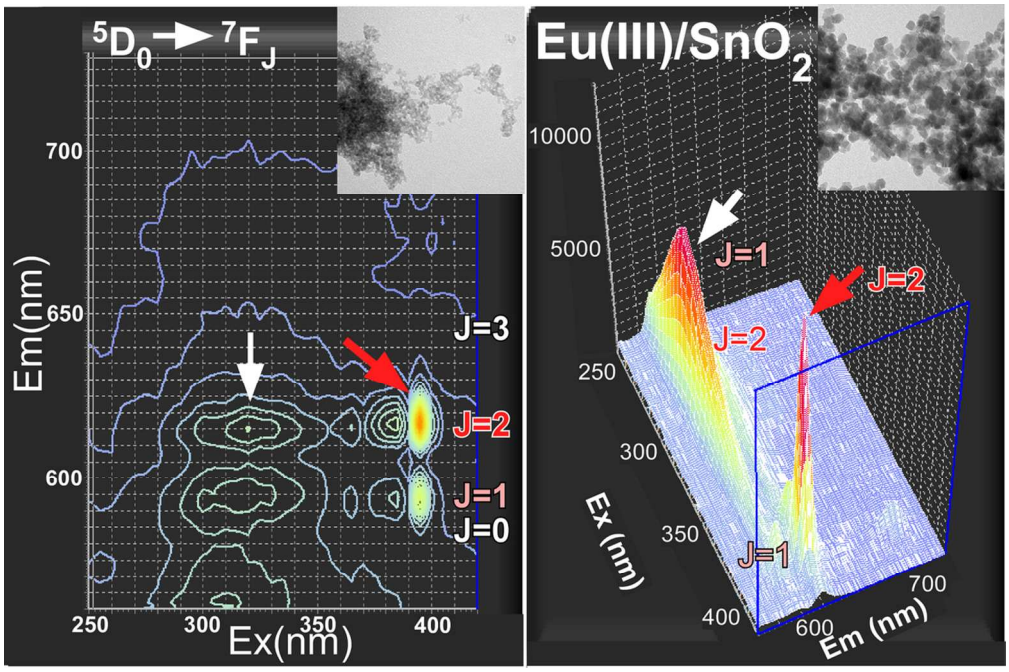

54x36mm (600 x 600 DPI)